

Synthetic Absorption Lines from Simulations of Multiphase Gas in Galactic Winds

LITA M. DE LA CRUZ,¹ EVAN E. SCHNEIDER,² AND EVE C. OSTRIKER¹

¹*Department of Astrophysical Sciences, Princeton University, 4 Ivy Lane, Princeton, NJ 08540, USA*

²*Department of Physics and Astronomy, University of Pittsburgh, 3941 O'Hara Street, Pittsburgh, PA 15260*

ABSTRACT

Supernova-driven galactic winds are multiphase streams of gas that are often observed flowing at a range of velocities out of star-forming regions in galaxies. In this study, we use high resolution 3D simulations of multiphase galactic winds modeled with the hydrodynamics code *Cholla* to investigate the connection between numerical studies and observations. Using a simulated interaction between a hot $T \sim 10^7$ K supernova-driven wind and a cool $T \sim 10^4$ K cloud of interstellar material, we create mock observables, including the optical depth and covering fraction of six commonly observed ions (Si II, C II, Si IV, C IV, N V, and O VI) as a function of gas velocity. We compare our mock observables to surveys of galactic winds in the literature, finding good agreement with velocities and profiles of the low ions. We then compute “empirical” values for the optical depth and covering fraction following observational techniques, and compare them to the values calculated directly from the simulation data. We find that the empirically computed values tend to underestimate the “true” value of τ for ions with high optical depth, and overestimate the “true” value of τ for ions with low optical depth, relative to the simulated data.

Keywords: galaxies: evolution - starburst - hydrodynamics - ISM: outflows - supernovae

1. INTRODUCTION

In 1963, an optical emission line spectrum revealed high velocity outflows of cool ionized gas in the central region of the nearby irregular galaxy M82 (Lynds & Sandage 1963). The large velocities indicated an outburst powered by a massive amount of energy - a phenomenon that has since captivated the interest of researchers for almost 60 years. Subsequent observations have revealed that outflows are common in star-forming galaxies, driven by the momentum and energy input of massive stars in the form of supernovae, stellar winds, cosmic rays, and radiation (see Heckman et al. 1993; Veilleux et al. 2005; Heckman & Thompson 2017; Veilleux et al. 2020, for reviews).

Outflows are now understood to play an important role in the evolution of galaxies and the intergalactic medium (IGM). By controlling the amount of gas in galaxies available to convert into stars, winds limit the baryon content of galaxies (Larson 1974; Somerville & Primack 1999; Kereš et al. 2005; Crain et al. 2009; Davé et al. 2011; Moster et al. 2013; Behroozi et al. 2013;

Genel et al. 2014; Muratov & Baulin 2015). By transporting metals out of star-forming regions, outflows regulate the metallicity of stars and gas in galaxies, setting the mass-metallicity relation (Tremonti et al. 2004). This same process enriches the circumgalactic medium (CGM) and intergalactic medium (IGM) with metals (Simcoe et al. 2004; Steidel et al. 2010; Werk et al. 2013; Rubin et al. 2014; Hopkins et al. 2014). Thus, understanding the process by which outflows remove gas from galaxies is key to understanding galaxy evolution.

Supernovae-driven winds are multiphase, and have been observed at a broad range of densities and temperatures (Heckman et al. 1990; Davé et al. 1998; Martin 2005; Strickland & Heckman 2009; Erb et al. 2012; Rubin et al. 2014). Generating a complete picture of multiphase winds, however, requires great time and effort and the use of many different observational instruments. With the high spatial resolution of the Chandra X-ray Observatory, the hot 10^7 K, supersonic wind created by supernova explosions can be observed directly, but only for the closest galaxies (Griffiths et al. 2000; Strickland & Heckman 2007). This phase in any case carries very little of the mass that eventually leaves galaxies, in spite of its role as a primary driver; only by interacting with

denser ISM phases is the hot, fast wind able to create a massive outflow.

The cooler ($T < 10^6$ K), indirectly accelerated gas in outflows is commonly studied by observers because of the many strong absorption and emission lines (Heckman et al. 2000). Given the n^2 dependence on density, detecting outflows in emission lines of distant galaxies tends to be challenging, so outflows in these sources are more typically studied via absorption lines. Measurements of absorption line profiles give direct insight into the velocity distribution and column density of the outflowing gas, as well as indirect measurements of metallicity, optical depth, covering fraction, and mass outflow rates. Commonly detected species in absorption include C, N, O, Mg, Ca, Si, S, and Fe. These species in their various ionization states probe a range of gas temperatures ranging from cold neutral gas ($T \sim 10^3$ K) to hot ionized gas ($T \sim 10^6$ K).

The installation of the Cosmic Origins Spectrograph (COS) on the Hubble Space Telescope (HST) significantly increased the efficiency of observations of this neutral and ionized gas phase in the outskirts of nearby UV bright starburst galaxies (Shull 2009; Green et al. 2012; Leitherer et al. 2013; Wood et al. 2015; Chisholm et al. 2015, 2016a,b, 2017). Tumlinson et al. (2011) and Thom et al. (2011) used COS to study the gaseous halos of low redshift galaxies and examined the metallicity and ionization of O VI absorption lines that surrounded these halos. In a particularly detailed observation of a gravitationally-lensed galaxy, Chisholm et al. (2018) studied the O VI doublet ($\lambda = 1032\text{\AA}$), one of the few observable tracers that is provisionally created during mass-loading (a mixing phase between the cool and hot gas). That study found that the O VI doublet is a unique species that has two regimes: at high velocity it mimics low-ionization optically thin lines, and at low velocity it mimics strong saturated lines. In many cases, the creation of this species is ambiguous, and it can be found in many different environments such as galaxies, the CGM, filaments, and the IGM (Savage et al. 1998; Tripp et al. 2001; Lehner et al. 2009; Werk et al. 2016).

There are many observational studies of the warm neutral and (photo)ionized 10^4 K gas in outflows, because this phase has strong absorption and emission lines in the rest-frame ultraviolet and optical (Heckman et al. 2000). Early optical emission line studies of galactic outflows used narrow-band images and long-slit spectroscopy of nearby edge-on bright IR galaxies (McCarthy et al. 1987; Heckman et al. 1990; Lehnert & Heckman 1996). Other observational work uses absorption lines from the Na I “D” doublet in far-IR starburst galaxies (Heckman et al. 2000; Martin 2005; Rupke et al.

2005a). Due to its low ionization potential of 5.1eV, ground state Na I D can effectively probe the neutral gas phase ($T \lesssim 8000$ K) in galactic winds. The ubiquity of this doublet in ultraluminous IR galaxies (ULIRGs) makes it a regularly used tracer in studies of these systems. However, this delicate species is shielded from photoionization by the immense amount of dust found in ULIRGS (Heckman et al. 2000, 2001; Martin 2006; Heckman & Thompson 2017), and is easily destroyed in less dusty systems. UV absorption lines that are redshifted into the optical, such as Mg II and Fe II, can be used to study outflows of gas at $T \sim 10^4$ K in higher redshift galaxies via stacking of spectra (Weiner et al. 2009; Maltby et al. 2019; Sugahara et al. 2019). These species can survive the strong UV radiation fields, but require high spectral resolution and individual observations generally require bright galaxies to achieve adequate signal-to-noise (Kornei et al. 2012; Rubin et al. 2014). In some unique cases, such as gravitationally lensed systems, these species can be studied in detail in high-redshift galaxies with lower star formation rates (Chisholm et al. 2018).

On the theoretical side too, much effort has been spent trying to understand the physics of galactic outflows. However, understanding the different processes that govern the different phases of gas has proven to be challenging. Early analytic work by Chevalier & Clegg (1985) provided a model of the observed X-ray emission produced by the directly-thermalized hot plasma in supernova-driven outflows. However, these spatially-resolved X-ray observations are limited to nearby galaxies, and are not easy to link to observations of other phases. In order to produce a complete theoretical picture, simulations must compare to the many down-the-barrel absorption line measurements used to study the lower-temperature gas in both local and more distant galaxies. But this approach too has challenges. Converting these absorption-line measurements into direct physical properties like mass outflow rates often requires a host of limiting assumptions. Likewise, converting simulated data into directly-observed quantities is non-trivial.

Numerical simulations can provide an avenue to better link our theoretical and observational models of outflows. In recent years, much theoretical work has focused specifically on understanding the physics that governs the interaction between a hot, supernova-driven wind and embedded cool clouds of material. In a seminal numerical study, Klein et al. (1994) formulated a characteristic timescale that describes the cloud-shock interaction: the cloud-crushing time t_{cc} . The cloud-crushing time roughly refers to the amount of time that it takes

the initial shock to propagate through the cloud. Analyzing 2D adiabatic simulations, Klein et al. (1994) used this timescale to describe the various stages of cloud evolution. The authors concluded that on large scales, spherical clouds in a background wind are destroyed in only a few t_{cc} . Subsequently, the cloud material mixes efficiently at $t \approx 4-5t_{cc}$ with the surrounding medium via small scale instabilities.

In subsequent years, different studies have focused on the different physical mechanisms that may affect this interaction, including magnetic fields (Mac Low et al. 1994; Gregori et al. 2000; Banda-Barragán et al. 2016), radiative cooling (Fragile et al. 2005; Cooper et al. 2009; Scannapieco & Brüggén 2015) and thermal conduction (Orlando et al. 2005; Brüggén & Scannapieco 2016). While these numerical works all contributed to our understanding of the cloud-wind interaction, almost all studies focusing on the problem of cloud acceleration and destruction studied either spherical or elliptical clouds.

Using extremely high-resolution simulations run with the GPU-based code *Cholla*, Schneider & Robertson (2015) explored the effects of spatial density distribution on the cloud-shock problem, following the evolution of both spherical clouds and of clouds with a lognormal density distribution set by turbulence. That study demonstrated that turbulent clouds are destroyed more quickly than spherical clouds of the same mass and mean density. In a followup study, Schneider & Robertson (2017) ran a series of radiative simulations that explored the interaction between a hot ($T = 10^6$ K) supernova-driven wind and a cool turbulent cloud representing entrained interstellar material.

Due to the extremely high spatial resolution afforded by *Cholla* and the realistic way that the turbulent clouds mix, these simulations are ideal for studying the phase structure of gas in outflows. After the initial shock, a wide distribution of densities and temperatures is created as gas in the cloud mixes with gas in the wind. This paper focuses on an analysis of those simulations at a characteristic time representative of an average state for a multiphase galactic wind. In particular, we analyze one of these cloud-wind simulations by creating mock absorption lines that can be compared to the plethora of observational data, thereby linking theoretical studies of cloud-wind interactions with observational studies of multiphase galactic outflows.

Section 2 describes the simulation of the interaction between a cool turbulent cloud and the hot wind. In Section 3 the physical properties of gas in the simulation are explored. Mock absorption lines are created for a variety of ionic species, and we compare different methods for

deriving values of the optical depth and covering fraction. In Section 4, we compare our results with previous observational and theoretical work. Finally, Section 5 briefly summarizes the paper.

2. THE CLOUD-WIND SIMULATION

In order to better understand the interaction between the hot and cool phases in outflows, Schneider & Robertson (2017) ran a high resolution simulation of a hot flow (with physical parameters modeling a supernova-driven wind) interacting with a cool, dense interstellar medium cloud. Below, we briefly describe the details of the simulation - a more extensive description can be found in the original work.

The simulation was run using *Cholla*, a GPU-based hydrodynamics code that allows for efficient computation (Schneider & Robertson 2015). The *Cholla* code uses an HLLC Riemann solver and PPM reconstruction, and for this simulation optically-thin radiative cooling was implemented using pre-computed Cloudy tables (Ferland et al. 2013). Cooling rates were calculated assuming solar metallicity for all the gas and cooling was allowed down to a temperature of $T = 10$ K. Allowing gas to cool to temperatures below $T = 10^4$ K allowed for greater cloud compression, and substantially altered the density distribution relative to previous studies. Heating from a metagalactic UV background was also included (Haardt & Madau 2012), although this does not make a practical difference to the thermodynamics for the regime studied. The simulation volume consists of a box with physical dimensions $160 \times 40 \times 40$ pc, with $2048 \times 512 \times 512$ cells, yielding a resolution of $\Delta x = 0.07825$ pc/cell. The numerical efficiency of *Cholla* enables this high resolution to be maintained across the entire simulation volume, allowing us to study mixing and cooling and the evolution of the gas through multiple phases and across a large region.

Properties for the background hot wind were set based on the Chevalier & Clegg (1985) spherical adiabatic solution, with an energy input rate $\dot{E} = 10^{42}$ erg s $^{-1}$, mass input rate $\dot{M} = 2M_{\odot}$ yr $^{-1}$, and driving region size $R_* = 300$ pc, as motivated by the Strickland & Heckman (2009) fit to Chandra X-ray observations of M82. The wind properties were set using the model solution at $r = 1$ kpc, giving a number density $n_{\text{wind}} = 5.26 \times 10^{-3}$ cm $^{-3}$, temperature $T = 3.7 \times 10^6$ K, and velocity $v_{\text{wind}} = 1.1962 \times 10^3$ kms $^{-1}$. Meanwhile, the cool component of the simulation is representative of interstellar material recently entrained in the hot outflow. This cool material is set to be initially at rest and in thermal pressure equilibrium with respect to the background wind. The distribution of interior densities is set to a

range of values as imposed by turbulence for Mach ~ 5 on the scale of the cloud (Schneider & Robertson 2017). The initial median density of the cloud is $\tilde{n} = 0.5$, rmmcm^{-3} and the median temperature is $T_{\text{med}} = 3.98 \times 10^4 \text{ K}$; the initial temperature distribution of the cloud is determined by the density. The cloud has an initial radius $R_{\text{cl}} = 5 \text{ pc}$, such that the column density of hydrogen through its center is $N_H = 1.02 \times 10^{20} \text{ cm}^{-2}$, and the total cloud mass is $8.61 M_{\odot}$. The median density and inhomogeneous structure of the cloud influence its overall evolution, including the efficiency of cooling and the time it takes to be destroyed. The cloud has a low enough density that self-gravity can be ignored.

To interpret and compare the results to previous models of cloud-wind interactions, we describe evolution in terms of the cloud-crushing time, t_{cc} (Klein et al. 1994). When the simulation starts, the wind drives a shock through the cloud, which causes the cool material to heat up and accelerate in the wind direction. The cloud-crushing time is an estimate of the time for the initial shock to propagate through the cloud and maximally compress it. This timescale can be calculated using the cloud-wind density ratio $\chi = \frac{n_{\text{cloud}}}{n_{\text{wind}}}$, the radius of the cloud R_{cloud} , and the wind velocity v_{wind} :

$$t_{\text{cc}} = \frac{\chi^{\frac{1}{2}} R_{\text{cloud}}}{v_{\text{wind}}}. \quad (1)$$

For the parameters of our simulation, $t_{\text{cc}} = 39.8 \text{ Kyr}$. The simulation was run for 1 Myr, equivalent to 25 cloud-crushing times. A real galactic wind would contain many clouds, at various stages of evolution; this simulation represents one small piece of that interaction.

3. RESULTS

We begin with an overview of the physical properties of the gas throughout the simulation. We then discuss how the gas is split into different temperature ranges to represent different ions, as are often observed in real multiphase winds. Next, we describe how synthetic absorption lines were computed and present profiles for each ion. In calculating the absorption lines, we apply techniques used in observations that use doublets to obtain optical depth and covering fraction. We then compare distributions of optical depth obtained via direct computation from the simulation, vs. those calculated using the empirically derived values.

3.1. Mass, Velocity, and Temperature Distribution

The cloud in this study reaches maximum compression at $t_{\text{cc}} = 2$ and completely disintegrates by $t_{\text{cc}} = 20$. We use $10t_{\text{cc}}$ for our analysis, as it represents an average state that adequately captures the mixing between the

cool and hot gas. Figure 1 shows a simulation snapshot at $10 t_{\text{cc}}$. The top panel shows column density projected on the $x - z$ plane. The lower panels show slices of the density, velocity and temperature through the center of the domain.

The cloud material accelerates as momentum is transferred from the hot wind, and enters the outflowing wind with a range of velocities, as can be observed in the velocity slice. The low density material within the original cloud accelerates much faster than the high density material, and we see that velocities are anticorrelated with density. The density slice shows that most of the volume is occupied by low density gas, while the high density gas is clumped together in small knots, generally seeded by the highest-density regions of the original turbulent cloud. The temperature slice shows that most of the volume is filled with high temperature gas at approximately $T = 10^{6.5} \text{ K}$, the temperature of the shocked hot wind. By contrast, the highest density regions remain at low temperature, driven by efficient radiative cooling of the highest density cloud gas. By volume, most of the gas in the simulation has a low density, high velocity, and high temperature, but it should be noted that this is partly driven by our selection of a small initial cloud.

The velocity distributions of the gas in the simulation can be quantified via one-dimensional histograms. The distribution of all the gas in the simulation is shown in Figure 2, in mass-weighted (top) and volume-weighted (bottom) 1D velocity histograms. The upper panel shows clear peaks that differentiate the cool and hot gas phases. By mass, about 90 % of the gas in the simulation is part of the hot wind (defined by an $T > 2 \times 10^4 \text{ K}$), as expected given the small initial cloud mass. At this particular cloud-crushing time of $10 t_{\text{cc}}$, we find that the total mass of gas at $T < 2 \times 10^4 \text{ K}$ is approximately 43% of the initial cloud mass. The hot wind moves at a high velocity, $\sim 1,000 \text{ km s}^{-1}$ to $1,250 \text{ km s}^{-1}$. The cooler gas, created by mixing with the cloud, has velocities in the range $30\text{-}200 \text{ km s}^{-1}$. The ratio of mass in low to high velocity components reflects our choice of cloud mass to the mass of hot gas that fits within the domain. The bottom panel in Figure 2 shows the relative contribution of the hot wind and cool cloud to the total volume in the simulation. We can see from this Figure that 40% of the gas is unaffected wind material moving at the initial velocity of $1,200 \text{ km s}^{-1}$.

As a simple way to map the gas in our simulation to different absorption lines, we follow Figure 6 in Tumlinson et al. (2017), in which temperature ranges for each ion are given based on the full width at half maximum (FWHM) surrounding the temperature associated with the peak abundance of that ionic species from collisional

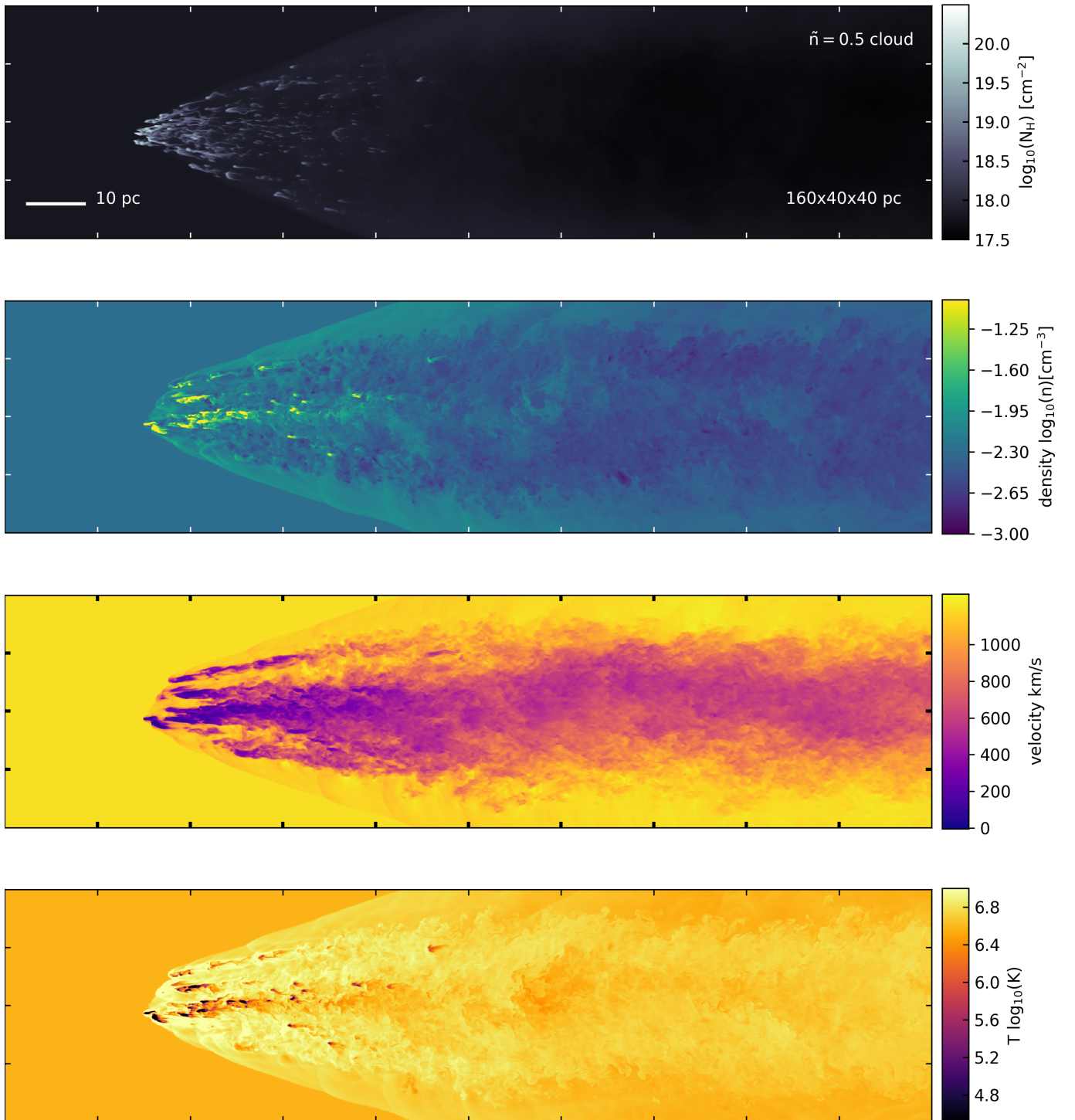


Figure 1. Mixing between the hot and cool gas is captured at an intermediate state of $t_{cc} = 10$. Panels show the projected column density, as well as slices of density, velocity, and temperature through the $x - z$ midplane.

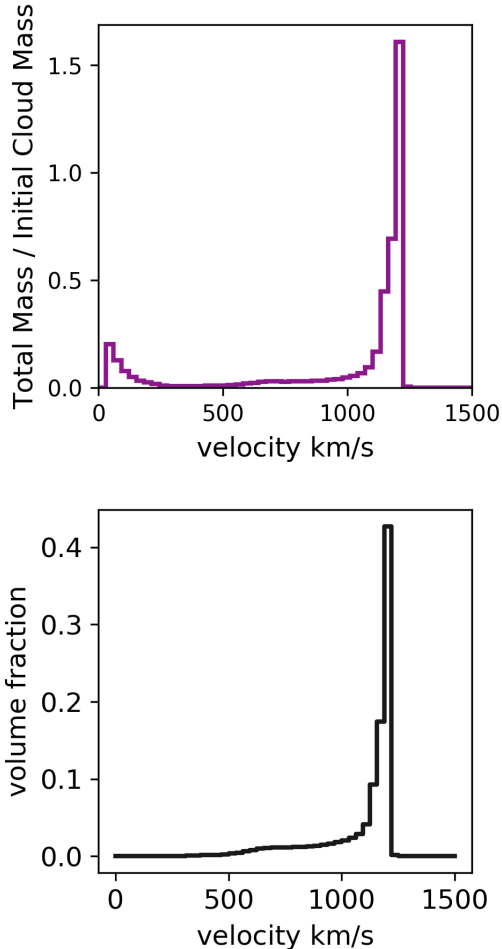


Figure 2. 1D mass-weighted (top panel) and volume-weighted (bottom panel) velocity histograms. The hot gas travels at high velocities ranging from 1,000 to 1,250 km s⁻¹ and comprises the majority of the mass and almost all of the volume. The cool cloud material occupies a negligible amount of space, but has a significant mass contribution.

ionization. Table 1 shows the range of temperatures adopted for each species in this study. Assigning ionization states in this way allows us to study the contribution of each ionic species to the total mass and volume throughout the simulation.

In Figure 3, we show mass-weighted 1D velocity histograms for a representative low, medium, and high ion constructed using these temperature ranges. In general, we see similar behavior between low, intermediate, and high ions, and find that Si II, C IV, and O VI are representative of other ions in those ranges. These histograms show that the higher ionization species contribute less to the total mass in the simulation. Furthermore, we see that the dense gas traced by the low ions has slower average velocities.

Table 1. Ionic Species Used in Absorption Line Analysis

Ion	$\log_{10}(T)$	$\lambda_{0,w}$	$\lambda_{0,s}$	f_w	f_s	$\frac{n}{n_H}$
Si II	3.8 - 4.3	1193	1260	0.5820	1.1800	$3.47e^{-5}$
C II	3.9 - 4.9	904	904	0.1680	0.3360	$2.45e^{-4}$
Si IV	4.6 - 5.2	1403	1394	0.2600	0.5240	$3.47e^{-5}$
C IV	4.9 - 5.3	1551	1548	0.0952	0.1900	$2.45e^{-4}$
N V	5.1 - 5.5	1243	1239	0.0777	0.1560	$8.51e^{-5}$
O VI	5.3 - 5.7	1038	1032	0.0658	0.1325	$4.90e^{-4}$

Col. 1: Ion Species

Col. 2: Gas temperature range [K], calculated using the full-width half max range for collisionally ionized gas (see e.g. Table 6 of [Tumlinson et al. \(2017\)](#))

Col. 3: Rest-wavelength for weak absorption lines.

Col. 4: Rest-wavelength for strong absorption lines.

Col. 5: Oscillator strength for weak absorption lines.

Col. 6: Oscillator strength for strong absorption lines.

Col. 7: Solar abundance (relative to hydrogen) for each ionic species.

Adopting the abundances in Table 1, Figure 4 shows maps of column density for the three representative low, medium, and high ions. In general, O VI tends to be more spatially extended than the low ionization ions. Still, the three ions trace each other fairly well, indicating that the gas giving rise to them is generally spatially related. This reinforces the idea that the intermediate and higher ionization species are primarily being created as a result of the mixing between the cool cloud and the hot wind.

3.2. Absorption Line Profiles

We study absorption line profiles of six ions that probe different temperatures. As demonstrated by the temperature slice in Figure 1, gas in the simulation has a range of temperatures from 10 – 10⁷ K. We create mock absorption line profiles using the optical depth of each ionic species, which reflects both total column densities in each map pixel (e.g. Figure 4) as well as the line-of-sight velocity distribution. The optical depth is computed adopting the Sobolev approximation, which gives τ in terms of the density and radial velocity gradient as

$$d\tau(v; y, z) = \frac{\pi e^2}{mc} f \lambda_0 n(v; x, y, z) \frac{dx}{dv}. \quad (2)$$

Here, the line-of-sight velocity gradient is taken to be in the direction of the background wind (x , in the simulation). The oscillator strength (f) and rest-wavelength (λ_0) of each of the six species investigated in this study can be found in Table 1. By integrating the number densities along the x -axis in bins of velocity, we can directly compute the optical depth along each line-of-sight, giving $n_y \times n_z = 262144$ independent sightlines through

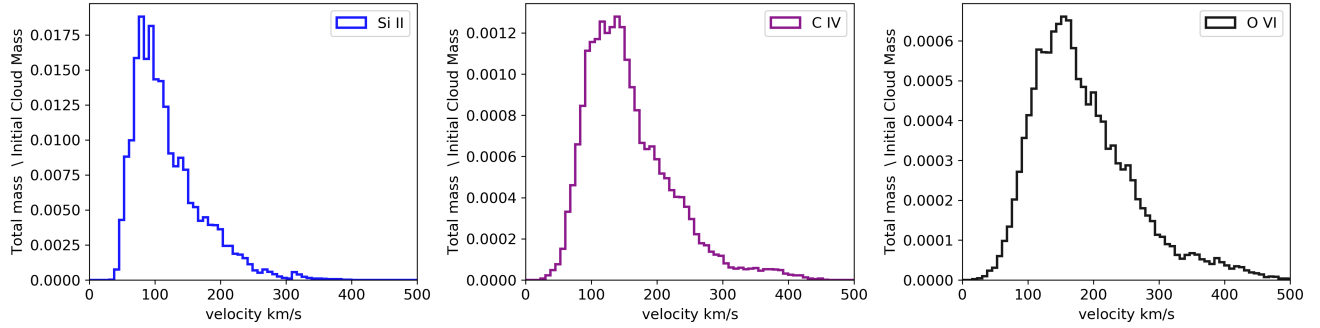


Figure 3. The distribution of mass with velocity for gas traced by a low, intermediate, and high temperature ion. The mass decreases for increasing temperature/ionization state, while the range of velocities increases.

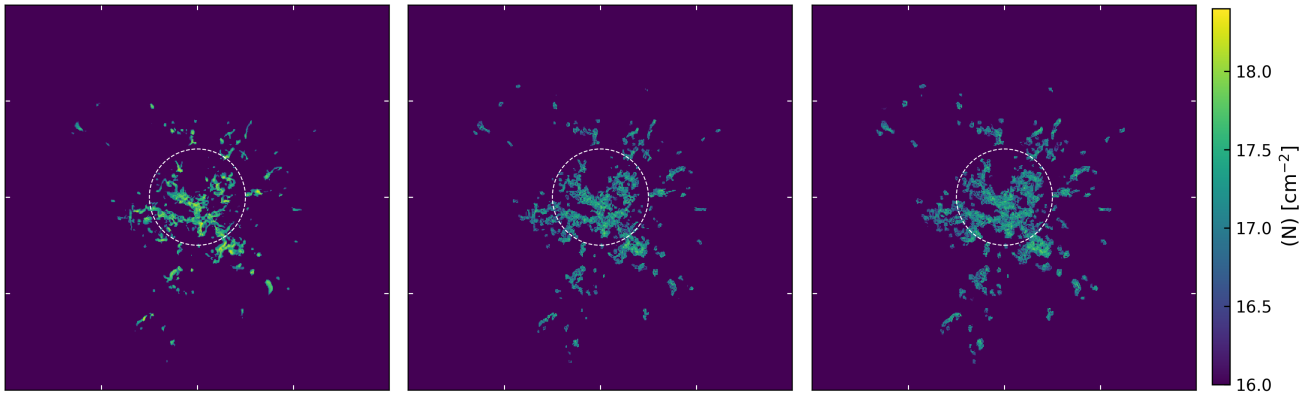


Figure 4. Column density maps of representative low, intermediate, and high temperature ions. The white dashed circle represents the original extent of the cloud in the simulation. The higher ions have slightly lower column densities and are slightly more spatially extended.

the simulation box. We use these to calculate the total flux decrements as a function of velocity for each species through the box; we shall also use the spatial distribution to assess covering factors.

The normalized observed flux $F(v)$ is defined as

$$F(v) = \frac{\int dydz e^{-\tau(v;y,z)} S}{\int dydz S} = \langle e^{-\tau(v)} \rangle_{yz}, \quad (3)$$

where S is the background source brightness (a stellar continuum) and where the average is over the $y-z$ projection of the simulation box. In the limit of low optical depth,

$$F(v) \approx 1 - \langle \tau(v) \rangle_{yz}; \quad (4)$$

from the definition of Equation 2 this involves spatial integration over the whole box. The flux decrement is then proportional to $M(v)$, the distribution of mass as a function of velocity traced by the ion.

Figure 5 shows the normalized flux as a function of velocity for the six ions in Table 1. Typically, down-the-barrel studies do not spatially resolve individual regions

of galaxies, and thus the absorption is a result of the integrated continuum and absorption across the entire central starburst region of a galaxy. For our normalized fluxes, the averaging is done over the entire box, so the size and mass of the cloud relative to the simulation box determines how much flux we observe. The larger the simulation box, the more unobstructed sight lines there are in the average, leading to shallower absorption lines. The bigger the clouds and the higher the column density, the more high τ sightlines enter the average, and the smaller the directly computed flux.

Three commonly measured features of absorption lines in winds are their minimum, central, and 90th percentile velocities. For each of the six ionic species, Table 2 lists v_{\min} , which is the velocity value corresponding to the minimum flux in the absorption line. v_{central} is a similar measurement, but is computed by first integrating the flux profiles (see Figure 5) from 0 to 1200 km/s and identifying the velocity at which we reach 50% of the area under the curve. Differences between v_{\min} and v_{central}

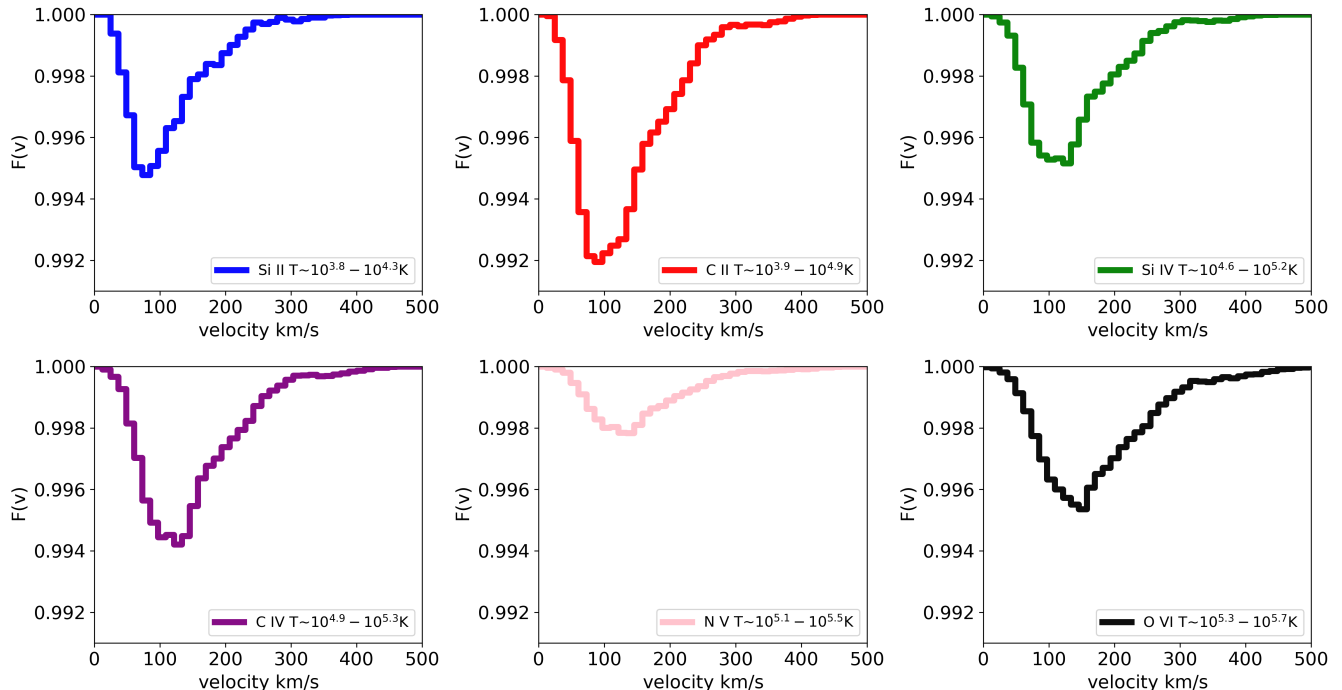


Figure 5. Normalized synthetic absorption line profiles for commonly-observed low, intermediate, and high ions. Table 2 lists the variation of v_{\min} , v_{central} , and v_{90} for each of the lines shown here.

Table 2. Velocity Properties of Synthetic Lines

Ions	Si II	C II	Si IV	C IV	N V	O VI
$v_{\min,s}$	85	97	133	133	145	158
$v_{\text{central},s}$	132	144	156	156	168	180
$v_{90,s}$	228	240	264	264	276	300

v_{\min} , velocity value corresponding to minimum flux value.

v_{central} , velocity value corresponding to 50% of the integrated flux.

v_{90} , velocity value that corresponding to 90% of the integrated flux.

give some idea as to the non-Gaussian skew of the absorption line - v_{central} is higher than v_{\min} for all of the lines, reflecting the extended high velocity tails. v_{90} is computed similarly to v_{central} with the exception that it identifies the velocity that corresponds to 90% of the area under the curve, giving a rough measure of the maximum (observable) velocity of the gas in the wind. Table 2 gives these values for each of our selected ions based on the profiles presented in Figure 5. From Table 2 we can see an increase in all three velocity statistics as we go from low ionization ions (Si II and C II) to high ionization ions (N V and O VI).

3.3. Empirical Covering Fraction and Optical Depth

The depth of an absorption line depends on both the optical depth τ and the covering factor C_f of the absorbing gas. The covering factor accounts for the fraction of background light source which is obscured by the

absorbing gas, while the optical depth measures the total amount of absorption in a given sight line as light passes through the cloud. For example, in Figure 5, the shape of the absorption lines is primarily determined by differences in τ as a function of velocity, while the overall normalization is set by the $y - z$ spatial extent of our cloud (see Figure 4). If lines are optically thin, the absorption profiles are essentially rescaled, inverted profiles $M(v)$, examples of which are shown in Figure 3. When $\tau > 3$ we define the line profile as optically thick, at which point the depth of the observed line will be set exclusively by C_f .

When the line profiles are optically thin, the depth of the line profiles becomes degenerate with C_f and τ . One observational technique to break this degeneracy and separately compute the optical depth and covering fraction takes advantage of doublets of the same ionic species. For example, Figure 6 shows strong and weak absorption lines for O VI. The strong line for O VI has a larger oscillator strength, f , and wavelength coefficients than the weak line. For doublets that have an f -value ratio equal to 2, the relationship between τ_s and τ_w becomes $\tau_s(v) = 2\tau_w(v)$. This unique ratio allows one to algebraically solve for the covering fraction independently of τ . In order to facilitate a comparison of our results with observations, we now present “empirical” estimates for the optical depth and covering fraction, derived according to this method. In all future

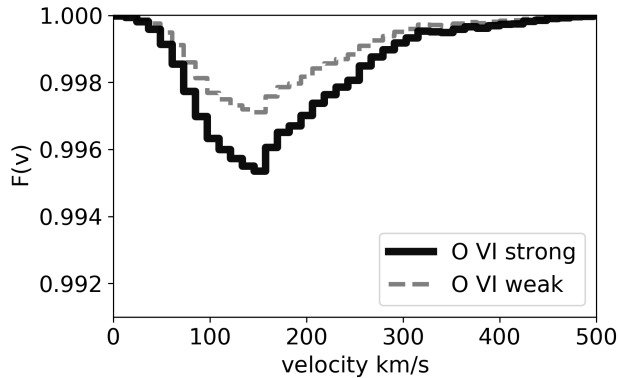


Figure 6. Strong and weak absorption lines for the O VI doublet. Although both the strong and weak line peak at the same v_{\min} the strong line has a larger τ , and deeper absorption.

discussion, “direct” will refer to the values calculated in Section 3.2, while “empirical” refers to values calculated using the following observational methodology.

Following Chisholm et al. (2018), empirical equations were derived for the optical depth and covering fraction of each ionic species. From Equation 3, if we consider a fraction $C_f(v)$ of the area as covered by a cloud with optical depth $\tau(v)$, and the remaining fraction $1 - C_f(v)$ as uncovered, the normalized flux would be

$$F(v) = 1 - C_f(v) + C_f(v)e^{-\tau(v)}. \quad (5)$$

If $\tau(v)$ for a weak and strong line is related by factor 2, the expression for the weak and strong line can be combined to solve for the covering fraction and the optical depth as a function of the flux in each line, assuming each line has the same C_f . The result is

$$C_f(v) = \frac{(1 - F_w(v))^2}{F_s(v) - 2F_w(v) + 1} \quad (6)$$

and

$$\tau_0(v) = \ln \left[\frac{1 - F_w(v)}{F_w(v) - F_s(v)} \right], \quad (7)$$

where F_w represents the flux from the weak line, F_s is the flux of the strong line, and $\tau_0(v)$ is the optical depth of the weak line.

We can use our directly computed flux for both strong and weak lines and Equation 6 to calculate an empirical estimate of the covering fraction of each species. In Figure 7, we show this empirically calculated covering fraction and compare it to the directly calculated covering fraction, computed by summing all the lines-of-sight with $\tau > 0.1$ and normalizing by the total number, $n_y \times n_z = 262144$ lines of sight along the x-direction. There is excellent agreement at all velocities for the low ions, and the modes of the distributions for the direct and empirical method are quite similar for all lines.

However, the empirically-calculated covering fractions tend to be slightly lower than the directly-computed values for intermediate and high temperature ions.

Figure 8 shows the empirically-calculated optical depth, $\tau_0(v)$, for the six different ions that were used for this study. The low ions, Si II and C II, have very similar optical depths. Si II peaks at $\tau_0 = 3.98$ and C II peaks at $\tau_0 = 3.41$; both of these ions also have the same peak velocity of 48 km/s. This similarity is of course primarily driven by the similar temperature ranges assigned to each ion, and their similar mass fractions under the assumption of solar relative abundances. From this Figure, we also see that the velocity range of the low ions is larger than would be captured by a measurement of v_{90} . That is, while most of the mass in these low ions is at low velocity, there is a tail of high velocity gas even at relatively cool temperatures. The intermediate and higher ions tend to have broader velocity ranges on the whole, and are optically thin across the entire range.

Figure 9 shows a comparison between the empirical and direct calculations of the optical depth for the weak lines. For the direct method the dashed lines show the median value of τ , while the bottom of the shaded region shows the 25th percentile and the upper boundary represents the 75th percentile. The empirically-calculated values are shown in solid lines. Examining the two upper left panels, we see that low ions tracing low temperature gas tend to have $\tau_0(v)$ values that underestimate the directly calculated value of τ . Conversely, in the panels that show our medium and high ions, the value of $\tau_0(v)$ consistently overestimates τ . Equation 7 can be used to quantitatively explain the cases when $\tau_0(v)$ under or over-estimates τ , as follows.

First, we rewrite Equation 7 in terms of the average flux deficit,

$$\tau_0(v) = \ln \left[\frac{1 - \langle e^{-\tau_w(v)} \rangle}{\langle e^{-\tau_w(v)} (1 - e^{-\tau_w(v)}) \rangle} \right]. \quad (8)$$

This equation can now be used to describe the two different behaviors of $\tau_0(v)$. We define two regimes of τ_0 as τ_{low} and τ_{high} , such that $\langle e^{-\tau_0} \rangle \sim (e^{-\tau_{\text{low}}} + e^{-\tau_{\text{high}}})/2$. These values are an arbitrary representation of the lower and upper 50th percentile of τ_0 . In the optically thick case where τ_{high} and $\tau_{\text{low}} \gg 1$,

$$\tau_0(v) \sim \ln \left[\frac{2}{e^{-\tau_{\text{high}}} + e^{-\tau_{\text{low}}}} \right] \sim \tau_{\text{low}}. \quad (9)$$

In the opposite, optically thin regime where τ_{high} and $\tau_{\text{low}} \ll 1$,

$$\tau_0(v) \sim \ln \left[1 + \frac{\tau_{\text{high}}^2 + \tau_{\text{low}}^2}{\tau_{\text{high}} + \tau_{\text{low}}} \right] \sim \tau_{\text{high}}. \quad (10)$$

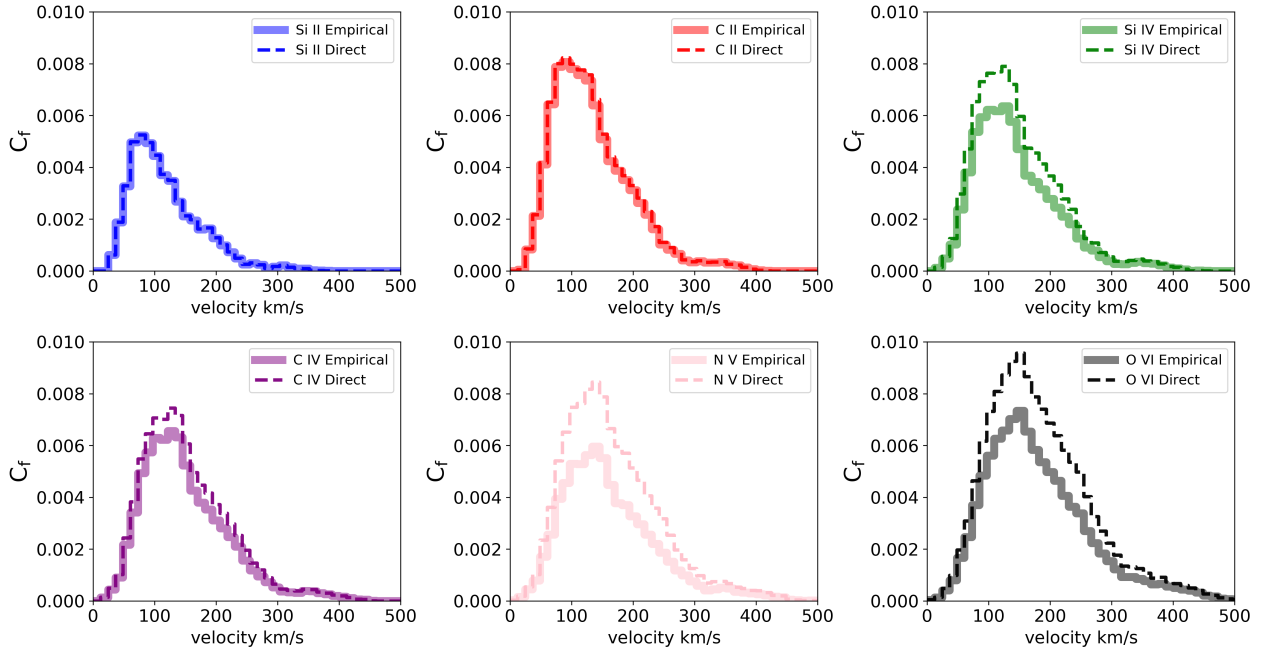


Figure 7. A comparison between the empirically derived and direct computation of the covering fraction for strong absorption lines. The empirical and direct method covering fraction calculations agree for low ionization ions, but for the intermediate and high ions the empirical method finds lower values for the covering fraction than the direct method calculation.

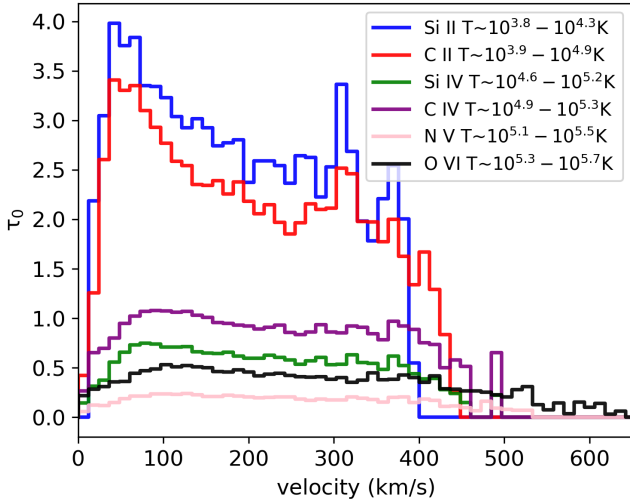


Figure 8. The empirical optical depth of doublets of six commonly used ionic species is shown. The lower ions tend to have higher optical depths, and peak at lower velocities.

Equations 9 and 10 can now be used to interpret Figure 9. Equation 9 shows that when optical depth is large, $\tau_0(v)$ tends to lie near the lower range of τ . Equation 10 shows that when optical depth is small, $\tau_0(v)$ tends to lie near the upper range of τ . Figure 9 shows that for the low ions such as Si II and C II that have direct values of $\tau > 1$, τ_0 indeed underestimates the true value of τ (shown by equation 9). Conversely, for the intermediate

and high ionization ions like Si IV, C IV, N V, and O VI, which are optically thin, τ_0 overestimates τ .

4. DISCUSSION

Developing a complete picture of galactic outflows requires a collaborative effort between theorists and observers. In order to interpret the results of numerical models in the context of observed systems, their properties must be translated into physical characteristics that can be observed directly, as demonstrated in Section 3. Before embarking on a comparison, however, we should note that the results of our numerical models depend critically on assumptions made about the physical properties of the gas in the simulation. In particular, the predetermined cloud and wind properties will affect the resulting absorption line profiles, covering fractions, etc. The range of cool gas velocities we see in the simulation depends on the initial velocity that is assigned to the hot wind, and potentially its density as well. Similarly, the optical depths and covering fractions values that are found in this study depend on the physical properties assigned to the cloud. Had we chosen a larger, or added multiple clouds along the line of sight, for example, the covering fraction and optical depth values would be larger. Furthermore, the comparison between our results and those from previous work are likely to differ due to different techniques and assumptions that are made. Of particular note is our assumption that all gas in the wind is in collisional ionization equilib-

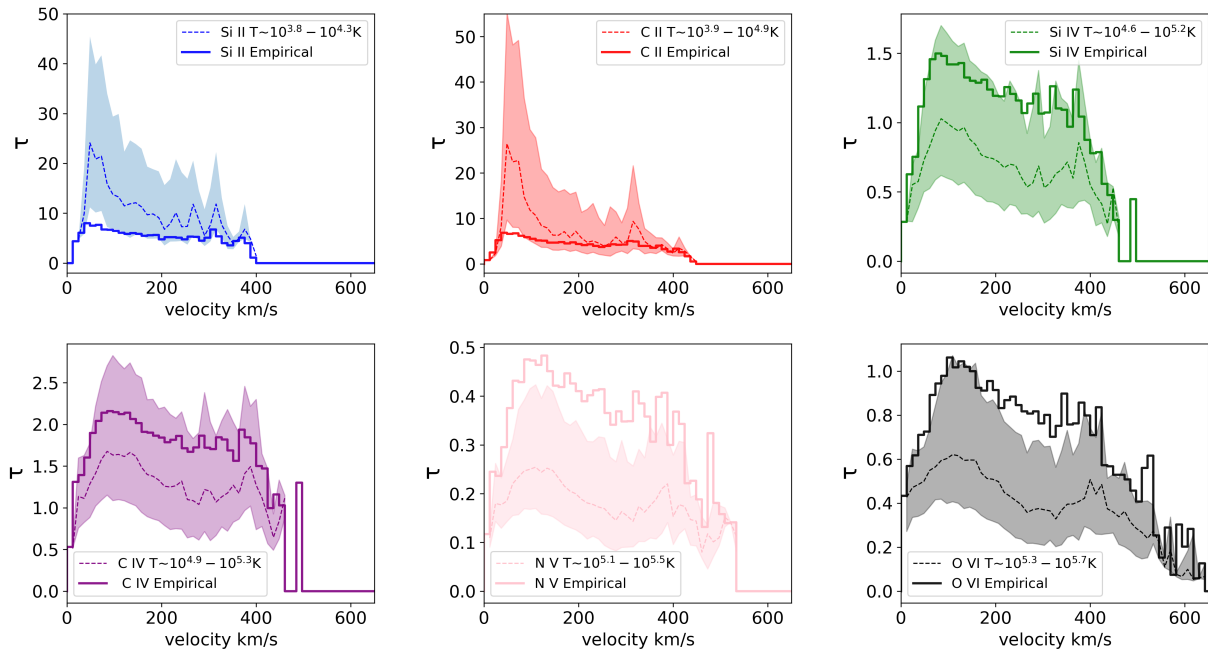


Figure 9. An optical depth (τ) comparison between six commonly used species that vary by temperature. The dashed line in each of the panels represents the median value of directly calculated τ . The shaded region represents the 25th and 75th percentile of the directly computed τ values for all sightlines. The solid colored lines represent the empirically calculated optical depth $\tau_0(v)$ for the strong lines.

rium. While this is a good starting point, it is likely that cool photoionized gas also contributes to the intermediate ions. This is an avenue we intend to investigate in future work.

4.1. Observational Comparison

The ubiquity of outflows and advancements in telescopes and instrumentation in recent years have made it possible to study this multiphase phenomenon with increasingly large samples of objects and with increasingly detailed spectroscopic coverage. Absorption line spectra, in particular, have been used to establish an understanding of the kinematics of galactic outflows as function of different ionic species. In this section, we compare our simulated absorption spectra and kinematics to several representative observational studies. Average characteristics of the galaxies in each study can be found in Table 3.

We begin our comparison with studies that focused on the Na I “D” absorption line (Heckman et al. 2000; Rupke et al. 2002, 2005b,a), which was used to study the warm neutral gas phase in starburst dominated, ultraluminous infrared galaxies (ULIRGs) and infrared galaxies (IRGs). Although we do not attempt to reproduce Na I “D” because of its sensitive dependence on the dust properties of the outflow, these studies are nevertheless a good example of early studies with large samples of objects displaying blueshifted absorption.

Heckman et al. (2000) investigated 32 far-IR-bright starburst galaxies drawn from parent samples in previous studies (Armus et al. 1989; Lehnert & Heckman 1995). The authors found that the absorption line profiles of Na I D in these outflow sources exhibit high maximum velocities that range from 400 to 600 km s⁻¹. In comparison to our lowest energy ions, we find that our maximum velocities for Si II of 400 km s⁻¹ and for C II of 448 km s⁻¹ are within the range of velocities computed in their study, although our v_{90} values tend to be significantly lower.

Using the ESI instrument on Keck II, Rupke et al. (2002) studied 11 ULIRG from the IRAS 1 Jy survey that have visible Na I D absorption. The authors measured a “typical” outflow speed of 300 km s⁻¹, which is consistent with our low ion values for v_{90} , but significantly higher than our values for $v_{central}$. Rupke et al. (2005b,a) studied 78 ULIRGs and IR-galaxies at $z < 0.5$. Because of the large sample size, the authors were able to study the evolution of winds as a function of host galaxy properties. The sample was split into three different categories: infrared galaxies (IRGs) ($z < 0.5$), low- z ULIRGs ($z < 0.25$), and high- z ULIRGs ($0.25 < z < 0.50$). ULIRGs, $L_{IR} > 10^{12}L_{\odot}$ are host to starbursts and power star formation with the large amount of dense molecular gas found in their cores. By contrast, IRGs ($10^{10}L_{\odot} < L_{IR} < 10^{12}L_{\odot}$) host fewer starbursts and have a lower wind detection rate than

Table 3. Characteristics of Galaxy Samples from the Literature

Reference	Absorption Lines	Sample Size	z	SFR ($M_{\odot}yr^{-1}$)
Heckman et al. (2000)	Na I D	32	< 0.1	10-100
Rupke et al. (2002)	Na I D	11	0.02-0.27	172-612
Rupke et al. (2005b,a)	Na I D	78	0.031, 0.129, 0.360	40, 225, 389
Weiner et al. (2009)	Mg II	1406 (stack)	1.4	10-50
Rubin et al. (2010)	Mg II, Fe II	468 (stack)	0.7-1.5	1 - 30
Rubin et al. (2014)	Mg II, Fe II	105	0.3-1.4	0.1-117
Heckman et al. (2015)	Si II-IV, Fe II, O I, Al II	19 of 39 (stack)	< 0.2	0.016-66
Chisholm et al. (2017)	Si IV	7	~ 0	0.02-26
Chisholm et al. (2018)	Si I-IV, Fe II, Al II-III, C II, C IV, N V, O I, O VI	1	2.9	< 48 ^a

^aWuyts et al. (2012)

ULIRGs (Heckman et al. 2000; Rupke et al. 2002; Martin 2005). Each of the three samples were selected from three different surveys; the IRGs from the the Infrared Astronomical Satellite (IRAS) Revised Bright Galaxy Sample (RBGS) and Warm Galaxy Sample (WGS), the low-z ULIRGs from the IRAS 1 Jy survey, and the high-z ULIRGs from the FIRST/FSC survey. We compare our maximum velocities for Si II and C II with the average maximum velocities for the three samples, which are 308, 401, and 359 km s⁻¹ for IRGs, low-z ULIRGs, and high-z ULIRGs respectively. Our maximum velocity for Si II (400 km s⁻¹) closely matches that of the low-z ULIRGs; while our maximum velocity for C II (448 km s⁻¹) exceeds the average maximum velocity computed in this study for all three samples.

Starting with stacks of galaxies at intermediate redshift, and later individual galaxies at lower redshifts, Weiner et al. (2009); Rubin et al. (2010, 2014); Heckman et al. (2015) used starburst galaxies to study UV absorption lines of the warm ionized gas (10⁴ – 10⁵ K) in outflows. Weiner et al. (2009) studied Mg II absorption in the stacked spectra of 1,406 starburst galaxies at z \sim 1.4 from the DEEP2 redshift survey. With an ionization potential of 15.0 eV, Mg II does not photodissociate as easily as Na I D which leads to smaller ionization corrections. This study found central outflow velocities that range from 250 to 300 km s⁻¹. Our v_{central} for Si II, C II, Si IV, and C IV are 132, 144, 156, 156 km s⁻¹ respectively, which are consistently smaller than the velocities found in this study. In a similar study, Rubin et al. (2010) investigated Mg II and Fe II absorption in the stacked spectra of 468 galaxies from the Team Keck Treasury Redshift Survey (TKRS) at slightly lower redshift. The authors found central velocity offsets of \sim 250 km s⁻¹ for Fe II and Mg II, with slightly larger offsets for Mg than Fe. These values are again slightly larger than our v_{central} values for the low ions.

Rubin et al. (2014) used redshift surveys of the Great Observatories Origins Deep Survey (GOODS) fields and the Extended Groth Strip (EGS) to analyze the individual spectra of 105 galaxies using the Mg II (λ 2796 and λ 2803) and Fe II (λ 2586 and λ 2600) doublet absorption line profiles at 0.3 < z < 1.4. Two distinct models were used in this study in order to quantify the kinematics and strength of each line profile. The “one-component” model follows the same approach as Rupke et al. (2005b) and parameterizes the normalized flux as a function of wavelength. The “two-component” model assumes that the same line profile comes from two velocities as opposed to one. We compare our v_{central} with the two-component model, for which most of the calculated v_{central} values are > 150 km s⁻¹, and find that our values for Si II, C II, Si IV, and C IV of 132, 144, 156, 156 km s⁻¹ respectively are within the range of velocity values calculated in this study.

Heckman et al. (2015) studied the kinematics of the warm gas phase found in supernovae driven winds of 39 low-redshift (z < 0.2) objects using UV absorption lines. This study used two samples of galaxies, the stacked spectra of 19 galaxies observed with the Far Ultraviolet Spectroscopic Explorer satellite (FUSE); and the individual spectra of 21 Lyman Break Analogs (LBAs) observed with COS on HST. We compare our absorption line profiles of Si II, C II, and Si IV with those computed in this study and find that our v_{min} values of 84, 96, 133 km s⁻¹ are systematically smaller than those found in this study. The v_{min} values that Heckman et al. (2015) find for the same species (Si II, C II, and Si IV) are 200, 150, 300 km s⁻¹ respectively.

Using COS spectra Chisholm et al. (2017) investigated 7 starburst galaxies using UV absorption lines. Using the Si IV doublet they derive and solve a system of two equations for the velocity-resolved optical depth and covering fraction, as described in Section 3. We compare our optical depth and covering fraction results

for Si IV to those from this study. The peak τ values for Si IV in this study range from $\tau \sim 0.5$ -2.7, comparable to our τ_0 value for Si IV which peaks at 0.75. A notable difference between our work and this study is the assumption in Chisholm et al. (2017) that the Si IV absorption is produced exclusively by cool photoionized gas, while we assume that it is produced exclusively by warm collisionally ionized gas. Our covering fractions are of course much smaller than those computed in this study due to the small area of the cloud in our simulation.

In a particularly instructive single-object study, Chisholm et al. (2018) used data from the the Magellan Evolution of Galaxies Spectroscopic and Ultraviolet Reference Atlas (MEGAsaURA) to study O VI 1032Å absorption from a gravitationally lensed high-redshift galaxy ($z \sim 2.9$) with a star formation rate of $< 48 M_{\odot}\text{yr}^{-1}$ as measured by SED fit. O VI in winds likely probes gas transitioning between a warm 10^4K gas and a hot $> 10^7\text{K}$, allowing the kinematics of distinct gas phases to be studied. This study examined absorption line profiles of many lower ions (see Table 3) and compared them to O VI, finding two “regimes” for the OVI line - at low velocities, its profile resembles that of the optically-thick low ions, while at high velocities its profile resembles that of the optically-thin lines. In general, we find that the optical depth of our lines is smaller than those shown in their work. This is partly due to the fact that the depth of our normalized flux is affected by the size of our simulation and the size of our cloud. When calculating our flux we average over the entire simulation box, so there are many unobstructed sight lines in our average, leading to shallow absorption lines. However, we can more fairly compare the quantities v_{central} and v_{90} from the studied metal absorption lines. In contrast to the previous studies mentioned, when comparing our computed velocity values to the derived quantities from Chisholm et al. (2018) we find that our values do not match the observations well. In this study the central velocities for the strong lines of Si II, C IV, and O VI are 201, 130, and 246 km s^{-1} while our values are systematically lower, at 132, 156, and 180 km s^{-1} respectively. Our v_{90} values for the same three species (228, 264, and 300 km s^{-1}) also underpredict those seen in this object - Chisholm et al. (2018) find values corresponding to these same species of 585, 455, and 532 km s^{-1} .

Generally speaking, our lowest ionization state gas appears to match the kinematics of the low- z observed absorption-line systems better than the high- z systems. Our numerical study is based on the canonical low- z starburst galaxy M82, and assumes a lower star forma-

tion rate (and thus less extreme hot wind properties) than many of the high- z systems discussed here, which may account for the better match to the systems observed a lower redshift. On the other hand, our higher ionization lines consistently underpredict the observed values for all studies. In particular, our higher ionization lines tend to have lower central and maximum velocities than those that are observed. In a number of recent studies, several authors have demonstrated that additional momentum can be transferred to gas in the warm photoionized phase and intermediate hotter phases via mixing with the hot wind, and that the amount of momentum transferred is a function of the amount of mixing that has occurred, and thus the distance that the gas has traveled (e.g. Gronke & Oh 2018, 2020; Fielding et al. 2018; Vijayan et al. 2020; Schneider et al. 2020). Because the simulation used in this study consisted of a small (5 pc) cloud in a relatively small (160 pc) box, there is simply not enough room for the higher ionization state gas to have achieved the velocities commonly observed. In larger scale simulations, this gas experiences further acceleration, and the higher ionization state profiles may be a better fit (Schneider et al. 2020). This is an avenue we will explore in future work.

4.2. Simulations

In addition to the many observational studies, the past couple of years has seen a substantial effort on the theoretical side to better understand the physics of outflows through the use numerical simulations (e.g Cooper et al. 2009; Scannapieco & Brügger 2015; Brügger & Scannapieco 2016; Schneider & Robertson 2017; Gronke & Oh 2018; Cottle et al. 2018; Kim & Ostriker 2018; Fielding et al. 2018; Kim et al. 2020). Most of these studies did not include absorption spectra and we therefore do not compare the results here, however, we can compare to Cottle et al. (2018), who included a thorough examination of blue-shifted absorption from an idealized wind simulation very similar to that presented in this work.

Cottle et al. (2018) used adaptive mesh refinement 3D hydrodynamic simulations from Scannapieco & Brügger (2015) and Brügger & Scannapieco (2016) to study a cool cloud in a hot wind. These simulations included the effects of radiative cooling, thermal conduction, and an ionizing background characteristic of a starburst galaxy in varying combinations. The authors used the TRIDENT code (Hummels et al. 2017) to produce synthetic column densities of 10 different species from the simulations: H I, Mg II, C II, C III, C IV, Si III, Si IV, N V, O VI, and Ne VIII. The physical volume of the simulation box hosting the interaction between these two phases is -800×800 pc along the x-y direction and -400×800

pc along the z direction which is the direction of the hot wind. The simulations used a cloud with an initial temperature of $T = 10^4\text{K}$, radius of $R_{\text{cloud}} = 100\text{pc}$, and a mass density of $\rho = 10^{-24}\text{g cm}^{-3}$ (substantially larger than the cloud in this work), and allowed cooling down to 10^4K . The study included results at four characteristic times in the cloud’s destruction that correspond to when 95%, 75%, 50%, and 25% of the mass fraction of the cloud remains at or above 1/3 of the cloud’s original density. Here we compare our results to their t_{50} which is the most similar to our 10 t_{cc} snapshots.

We compare our column densities of C IV and O VI to those computed in this study and find that similar to our findings O VI tends to be more spatially extended than the lower ions. As in our simulation, the column density profiles of all the ions in Cottle et al. (2018) trace each other fairly well indicating that the species are spatially related and have a similar creation mechanism. Comparing to our normalized flux results, we find similar results only for N V - all other ions in our study have much smaller depths than theirs, and their lowest ionization states are completely saturated. This can primarily be attributed to the much larger cloud used in the Cottle et al. (2018) work, which leads to larger column densities, optical depths, and covering fractions. When comparing our velocities with those in this study we see that for both our model and Cottle et al. (2018) the velocities increase with ionization state. This stands in contrast to the velocities shown in Chisholm et al. (2018) Table 1, where there is not a clear correlation between increasing ionization states and velocities. Additionally, we compare our covering fraction results to those from this study and find that our values are smaller than those presented in this study. Although our velocity profiles do not have a similar shape to those presented in Cottle et al. (2018), we do find similar v_{min} values - our velocities all fall within their peak range of ~ 50 to 200 km s^{-1} for the various ions.

5. CONCLUSIONS

In this work, we have presented a study of the gas in multiphase outflows using a high resolution numerical simulation that models the interaction between a hot supernovae driven wind and cool cloud of interstellar material (Schneider & Robertson 2017). Using this simulated dataset, we have created observables that we compare to observational studies of outflows, in order to better understand the kinematics and phase structure of the gas. Gas in the simulation has a wide range of temperatures, densities, and velocities. By assigning ionization states to the gas using collisionally ionized gas temperatures, we enable a direct comparison to the

individual species observed in absorption line studies of outflows.

In particular, we create synthetic absorption lines for a sample of representative ions, which are then used to calculate the optical depth and covering fraction of individual species. These absorption lines are characterized by a few general features: as ionization state increases so do velocity centroids and maximum values (see Table 2). Optical depths are higher for the lower ions, and covering fractions are lower, although marginally. All of our covering fractions are very low compared to the observations, which is a result of our small cloud size compared to the simulation domain. Consequently, the absorption as shown by the normalized fluxes presented in this work is very shallow relative to observed lines. We therefore focus primarily on the shapes of the velocity profiles and associated statistics.

Motivated by Chisholm et al. (2018) we also derived an “empirical” optical depth and covering fraction using doublets from the same ionic species. We compared these values with the directly computed optical depth and covering fraction values obtained using the simulation. Figure 9 shows that the empirically derived optical depth for the optically-thick low ionization ions like Si II and C II tends to underestimate the true values of τ . Conversely, the empirical optical depth values for the intermediate and high ions overestimates the true value of τ . It is nevertheless true that the “empirical” optical depth is still between the 25th and 75th percentile of the optical depth distribution for most ions. We demonstrate that biases in optical depth estimates can be understood based on whether the absorption lines are optically thick or optically thin (see Eqns 9 and 10).

In Section 4, we compare our results with an extensive sample of observational studies from the literature that investigate line profiles of species with similar ionization states (e.g Na I D, Mg II, and Fe II). We find that that our maximum velocity for Si II and C II resembles the velocities reached by Na I D. Similarly, our central velocities for Si II, C II, Si IV, and C IV are within the typical velocity ranges of most UV absorption line studies, particularly for lower star formation rate systems more comparable to our assumed wind. Our higher ionization lines undershoot the maximum velocities reported in most systems, which is a result of our small simulation box size and limited physical range for acceleration.

This study is an first step towards more detailed comparisons of simulated and observed absorption line data. In future work, we hope to expand the results of this work to larger simulations, and improve the physical accuracy of the simulated absorption lines through full radiative-transfer modeling. Nevertheless, we anticipate

that the results presented here will provide additional insight into the nature of the multiphase gas in galactic outflows, and how it gives rise to the observed fluxes. These comparisons between simulated data and observations will ultimately help improve both our theoretical models and our ability to interpret the kinematics of galactic outflows.

6. ACKNOWLEDGMENTS

This research used resources of the Oak Ridge Leadership Computing Facility, which is a DOE Office of Science User Facility supported under Contract DE-AC05-00OR22725, via an award of computing time on the Ti-

tan system provided by the INCITE program (AST125). E.E.S was supported in part by NASA through Hubble Fellowship grant #HF-51397.001-A awarded by the Space Telescope Science Institute, which is operated by the Association of Universities for Research in Astronomy, Inc., for NASA, under contract NAS 5-26555. The work of ECO was partly supported by grant 510940 from the Simons Foundation.

Software: Cholla (Schneider & Robertson 2015); matplotlib (Hunter 2007), numpy (van der Walt et al. 2011), hdf5

REFERENCES

- Armus, L., Heckman, T. M., & Miley, G. K. 1989, *ApJ*, 347, 727, doi: [10.1086/168164](https://doi.org/10.1086/168164)
- Banda-Barragán, W. E., Parkin, E. R., Federrath, C., Crocker, R. M., & Bicknell, G. V. 2016, *MNRAS*, 455, 1309, doi: [10.1093/mnras/stv2405](https://doi.org/10.1093/mnras/stv2405)
- Behroozi, P. S., Wechsler, R. H., & Conroy, C. 2013, *ApJ*, 770, 57, doi: [10.1088/0004-637X/770/1/57](https://doi.org/10.1088/0004-637X/770/1/57)
- Brüggen, M., & Scannapieco, E. 2016, *ApJ*, 822, 31, doi: [10.3847/0004-637X/822/1/31](https://doi.org/10.3847/0004-637X/822/1/31)
- Chevalier, R. A., & Clegg, A. W. 1985, *Nature*, 317, 44, doi: [10.1038/317044a0](https://doi.org/10.1038/317044a0)
- Chisholm, J., Bordoloi, R., Rigby, J. R., & Bayliss, M. 2018, *MNRAS*, 474, 1688, doi: [10.1093/mnras/stx2848](https://doi.org/10.1093/mnras/stx2848)
- Chisholm, J., Tremonti, C. A., Leitherer, C., & Chen, Y. 2017, *MNRAS*, 469, 4831, doi: [10.1093/mnras/stx1164](https://doi.org/10.1093/mnras/stx1164)
- Chisholm, J., Tremonti, C. A., Leitherer, C., Chen, Y., & Wofford, A. 2016a, *MNRAS*, 457, 3133, doi: [10.1093/mnras/stw178](https://doi.org/10.1093/mnras/stw178)
- Chisholm, J., Tremonti, C. A., Leitherer, C., et al. 2015, *ApJ*, 811, 149, doi: [10.1088/0004-637X/811/2/149](https://doi.org/10.1088/0004-637X/811/2/149)
- Chisholm, J., Tremonti Christy, A., Leitherer, C., & Chen, Y. 2016b, *MNRAS*, 463, 541, doi: [10.1093/mnras/stw1951](https://doi.org/10.1093/mnras/stw1951)
- Cooper, J. L., Bicknell, G. V., Sutherland, R. S., & Bland-Hawthorn, J. 2009, *ApJ*, 703, 330, doi: [10.1088/0004-637X/703/1/330](https://doi.org/10.1088/0004-637X/703/1/330)
- Cottle, J. N., Scannapieco, E., & Brüggen, M. 2018, *ApJ*, 864, 96, doi: [10.3847/1538-4357/aad55c](https://doi.org/10.3847/1538-4357/aad55c)
- Crain, R. A., Theuns, T., Dalla Vecchia, C., et al. 2009, *MNRAS*, 399, 1773, doi: [10.1111/j.1365-2966.2009.15402.x](https://doi.org/10.1111/j.1365-2966.2009.15402.x)
- Davé, R., Hellsten, U., Hernquist, L., Katz, N., & Weinberg, D. H. 1998, *ApJ*, 509, 661, doi: [10.1086/306524](https://doi.org/10.1086/306524)
- Davé, R., Oppenheimer, B. D., & Finlator, K. 2011, *MNRAS*, 415, 11, doi: [10.1111/j.1365-2966.2011.18680.x](https://doi.org/10.1111/j.1365-2966.2011.18680.x)
- Erb, D. K., Quider, A. M., Henry, A. L., & Martin, C. L. 2012, *ApJ*, 759, 26, doi: [10.1088/0004-637X/759/1/26](https://doi.org/10.1088/0004-637X/759/1/26)
- Ferland, G. J., Porter, R. L., van Hoof, P. A. M., et al. 2013, *RMxAA*, 49, 137. <https://arxiv.org/abs/1302.4485>
- Fielding, D., Quataert, E., & Martizzi, D. 2018, *MNRAS*, 481, 3325, doi: [10.1093/mnras/sty2466](https://doi.org/10.1093/mnras/sty2466)
- Fragile, P. C., Anninos, P., Gustafson, K., & Murray, S. D. 2005, *ApJ*, 619, 327, doi: [10.1086/426313](https://doi.org/10.1086/426313)
- Genel, S., Vogelsberger, M., Springel, V., et al. 2014, *MNRAS*, 445, 175, doi: [10.1093/mnras/stu1654](https://doi.org/10.1093/mnras/stu1654)
- Green, J. C., Froning, C. S., Osterman, S., et al. 2012, *ApJ*, 744, 60, doi: [10.1088/0004-637X/744/1/60](https://doi.org/10.1088/0004-637X/744/1/60)
- Gregori, G., Miniati, F., Ryu, D., & Jones, T. W. 2000, arXiv e-prints, astro. <https://arxiv.org/abs/astro-ph/0006240>
- Griffiths, R. E., Ptak, A., Feigelson, E. D., et al. 2000, *Science*, 290, 1325, doi: [10.1126/science.290.5495.1325](https://doi.org/10.1126/science.290.5495.1325)
- Gronke, M., & Oh, S. P. 2018, *MNRAS*, 480, L111, doi: [10.1093/mnrasl/sly131](https://doi.org/10.1093/mnrasl/sly131)
- . 2020, *MNRAS*, 492, 1970, doi: [10.1093/mnras/stz3332](https://doi.org/10.1093/mnras/stz3332)
- Haardt, F., & Madau, P. 2012, *ApJ*, 746, 125, doi: [10.1088/0004-637X/746/2/125](https://doi.org/10.1088/0004-637X/746/2/125)
- Heckman, T. M., Alexandroff, R. M., Borthakur, S., Overzier, R., & Leitherer, C. 2015, *ApJ*, 809, 147, doi: [10.1088/0004-637X/809/2/147](https://doi.org/10.1088/0004-637X/809/2/147)
- Heckman, T. M., Armus, L., & Miley, G. K. 1990, *ApJS*, 74, 833, doi: [10.1086/191522](https://doi.org/10.1086/191522)
- Heckman, T. M., Lehnert, M. D., & Armus, L. 1993, *Astrophysics and Space Science Library*, Vol. 188, Galactic Superwinds, ed. J. M. Shull & H. A. Thronson, 455, doi: [10.1007/978-94-011-1882-8_25](https://doi.org/10.1007/978-94-011-1882-8_25)
- Heckman, T. M., Lehnert, M. D., Strickland, D. K., & Armus, L. 2000, *ApJS*, 129, 493, doi: [10.1086/313421](https://doi.org/10.1086/313421)
- Heckman, T. M., Sembach, K. R., Meurer, G. R., et al. 2001, *ApJ*, 558, 56, doi: [10.1086/322475](https://doi.org/10.1086/322475)

- Heckman, T. M., & Thompson, T. A. 2017, arXiv e-prints, arXiv:1701.09062. <https://arxiv.org/abs/1701.09062>
- Hopkins, P. F., Kereš, D., Oñorbe, J., et al. 2014, MNRAS, 445, 581, doi: [10.1093/mnras/stu1738](https://doi.org/10.1093/mnras/stu1738)
- Hummels, C. B., Smith, B. D., & Silvia, D. W. 2017, ApJ, 847, 59, doi: [10.3847/1538-4357/aa7e2d](https://doi.org/10.3847/1538-4357/aa7e2d)
- Hunter, J. D. 2007, Computing in Science and Engineering, 9, 90, doi: [10.1109/MCSE.2007.55](https://doi.org/10.1109/MCSE.2007.55)
- Kereš, D., Katz, N., Weinberg, D. H., & Davé, R. 2005, MNRAS, 363, 2, doi: [10.1111/j.1365-2966.2005.09451.x](https://doi.org/10.1111/j.1365-2966.2005.09451.x)
- Kim, C.-G., & Ostriker, E. C. 2018, ApJ, 853, 173, doi: [10.3847/1538-4357/aaa5ff](https://doi.org/10.3847/1538-4357/aaa5ff)
- Kim, C.-G., Ostriker, E. C., Somerville, R. S., et al. 2020, arXiv e-prints, arXiv:2006.16315. <https://arxiv.org/abs/2006.16315>
- Klein, R. I., McKee, C. F., & Colella, P. 1994, ApJ, 420, 213, doi: [10.1086/173554](https://doi.org/10.1086/173554)
- Kornei, K. A., Shapley, A. E., Martin, C. L., et al. 2012, ApJ, 758, 135, doi: [10.1088/0004-637X/758/2/135](https://doi.org/10.1088/0004-637X/758/2/135)
- Larson, R. B. 1974, MNRAS, 169, 229, doi: [10.1093/mnras/169.2.229](https://doi.org/10.1093/mnras/169.2.229)
- Lehner, N., Prochaska, J. X., Kobulnicky, H. A., et al. 2009, ApJ, 694, 734, doi: [10.1088/0004-637X/694/2/734](https://doi.org/10.1088/0004-637X/694/2/734)
- Lehnert, M. D., & Heckman, T. M. 1995, ApJS, 97, 89, doi: [10.1086/192137](https://doi.org/10.1086/192137)
- . 1996, ApJ, 462, 651, doi: [10.1086/177180](https://doi.org/10.1086/177180)
- Leitherer, C., Chandar, R., Tremonti, C. A., Wofford, A., & Schaerer, D. 2013, ApJ, 772, 120, doi: [10.1088/0004-637X/772/2/120](https://doi.org/10.1088/0004-637X/772/2/120)
- Lynds, C. R., & Sandage, A. R. 1963, ApJ, 137, 1005, doi: [10.1086/147579](https://doi.org/10.1086/147579)
- Mac Low, M.-M., McKee, C. F., Klein, R. I., Stone, J. M., & Norman, M. L. 1994, ApJ, 433, 757, doi: [10.1086/174685](https://doi.org/10.1086/174685)
- Maltby, D. T., Almaini, O., McLure, R. J., et al. 2019, MNRAS, 489, 1139, doi: [10.1093/mnras/stz2211](https://doi.org/10.1093/mnras/stz2211)
- Martin, C. L. 2005, ApJ, 621, 227, doi: [10.1086/427277](https://doi.org/10.1086/427277)
- . 2006, ApJ, 647, 222, doi: [10.1086/504886](https://doi.org/10.1086/504886)
- McCarthy, P. J., van Breugel, W., & Heckman, T. 1987, AJ, 93, 264, doi: [10.1086/114309](https://doi.org/10.1086/114309)
- Moster, B. P., Naab, T., & White, S. D. M. 2013, MNRAS, 428, 3121, doi: [10.1093/mnras/sts261](https://doi.org/10.1093/mnras/sts261)
- Muratov, A., & Baulin, V. A. 2015, arXiv e-prints, arXiv:1511.09076. <https://arxiv.org/abs/1511.09076>
- Orlando, S., Peres, G., Reale, F., et al. 2005, A&A, 444, 505, doi: [10.1051/0004-6361:20052896](https://doi.org/10.1051/0004-6361:20052896)
- Rubin, K. H. R., Prochaska, J. X., Koo, D. C., et al. 2014, ApJ, 794, 156, doi: [10.1088/0004-637X/794/2/156](https://doi.org/10.1088/0004-637X/794/2/156)
- Rubin, K. H. R., Weiner, B. J., Koo, D. C., et al. 2010, ApJ, 719, 1503, doi: [10.1088/0004-637X/719/2/1503](https://doi.org/10.1088/0004-637X/719/2/1503)
- Rupke, D. S., Veilleux, S., & Sanders, D. B. 2002, ApJ, 570, 588, doi: [10.1086/339789](https://doi.org/10.1086/339789)
- . 2005a, ApJS, 160, 115, doi: [10.1086/432889](https://doi.org/10.1086/432889)
- . 2005b, ApJS, 160, 87, doi: [10.1086/432886](https://doi.org/10.1086/432886)
- Savage, B. D., Tripp, T. M., & Lu, L. 1998, AJ, 115, 436, doi: [10.1086/300222](https://doi.org/10.1086/300222)
- Scannapieco, E., & Brügggen, M. 2015, ApJ, 805, 158, doi: [10.1088/0004-637X/805/2/158](https://doi.org/10.1088/0004-637X/805/2/158)
- Schneider, E. E., Ostriker, E. C., Robertson, B. E., & Thompson, T. A. 2020, ApJ, 895, 43, doi: [10.3847/1538-4357/ab8ae8](https://doi.org/10.3847/1538-4357/ab8ae8)
- Schneider, E. E., & Robertson, B. E. 2015, ApJS, 217, 24, doi: [10.1088/0067-0049/217/2/24](https://doi.org/10.1088/0067-0049/217/2/24)
- . 2017, ApJ, 834, 144, doi: [10.3847/1538-4357/834/2/144](https://doi.org/10.3847/1538-4357/834/2/144)
- Shull, J. M. 2009, in American Institute of Physics Conference Series, Vol. 1135, American Institute of Physics Conference Series, ed. M. E. van Steenberg, G. Sonneborn, H. W. Moos, & W. P. Blair, 301–308, doi: [10.1063/1.3154069](https://doi.org/10.1063/1.3154069)
- Simcoe, R. A., Sargent, W. L. W., & Rauch, M. 2004, ApJ, 606, 92, doi: [10.1086/382777](https://doi.org/10.1086/382777)
- Somerville, R. S., & Primack, J. R. 1999, MNRAS, 310, 1087, doi: [10.1046/j.1365-8711.1999.03032.x](https://doi.org/10.1046/j.1365-8711.1999.03032.x)
- Steidel, C. C., Erb, D. K., Shapley, A. E., et al. 2010, ApJ, 717, 289, doi: [10.1088/0004-637X/717/1/289](https://doi.org/10.1088/0004-637X/717/1/289)
- Strickland, D. K., & Heckman, T. M. 2007, ApJ, 658, 258, doi: [10.1086/511174](https://doi.org/10.1086/511174)
- . 2009, ApJ, 697, 2030, doi: [10.1088/0004-637X/697/2/2030](https://doi.org/10.1088/0004-637X/697/2/2030)
- Sugahara, Y., Ouchi, M., Harikane, Y., et al. 2019, ApJ, 886, 29, doi: [10.3847/1538-4357/ab49fe](https://doi.org/10.3847/1538-4357/ab49fe)
- Thom, C., Werk, J. K., Tumlinson, J., et al. 2011, ApJ, 736, 1, doi: [10.1088/0004-637X/736/1/1](https://doi.org/10.1088/0004-637X/736/1/1)
- Tremonti, C. A., Heckman, T. M., Kauffmann, G., et al. 2004, ApJ, 613, 898, doi: [10.1086/423264](https://doi.org/10.1086/423264)
- Tripp, T. M., Giroux, M. L., Stocke, J. T., Tumlinson, J., & Oegerle, W. R. 2001, ApJ, 563, 724, doi: [10.1086/323965](https://doi.org/10.1086/323965)
- Tumlinson, J., Peeples, M. S., & Werk, J. K. 2017, ARA&A, 55, 389, doi: [10.1146/annurev-astro-091916-055240](https://doi.org/10.1146/annurev-astro-091916-055240)
- Tumlinson, J., Werk, J. K., Thom, C., et al. 2011, ApJ, 733, 111, doi: [10.1088/0004-637X/733/2/111](https://doi.org/10.1088/0004-637X/733/2/111)
- van der Walt, S., Colbert, S. C., & Varoquaux, G. 2011, Computing in Science and Engineering, 13, 22, doi: [10.1109/MCSE.2011.37](https://doi.org/10.1109/MCSE.2011.37)
- Veilleux, S., Cecil, G., & Bland-Hawthorn, J. 2005, ARA&A, 43, 769, doi: [10.1146/annurev.astro.43.072103.150610](https://doi.org/10.1146/annurev.astro.43.072103.150610)
- Veilleux, S., Maiolino, R., Bolatto, A. D., & Aalto, S. 2020, A&A Rv, 28, 2, doi: [10.1007/s00159-019-0121-9](https://doi.org/10.1007/s00159-019-0121-9)

- Vijayan, A., Kim, C.-G., Armillotta, L., Ostriker, E. C., & Li, M. 2020, *ApJ*, 894, 12, doi: [10.3847/1538-4357/ab8474](https://doi.org/10.3847/1538-4357/ab8474)
- Weiner, B. J., Coil, A. L., Prochaska, J. X., et al. 2009, *ApJ*, 692, 187, doi: [10.1088/0004-637X/692/1/187](https://doi.org/10.1088/0004-637X/692/1/187)
- Werk, J. K., Prochaska, J. X., Thom, C., et al. 2013, *ApJS*, 204, 17, doi: [10.1088/0067-0049/204/2/17](https://doi.org/10.1088/0067-0049/204/2/17)
- Werk, J. K., Prochaska, J. X., Cantalupo, S., et al. 2016, *ApJ*, 833, 54, doi: [10.3847/1538-4357/833/1/54](https://doi.org/10.3847/1538-4357/833/1/54)
- Wood, C. M., Tremonti, C. A., Calzetti, D., et al. 2015, *MNRAS*, 452, 2712, doi: [10.1093/mnras/stv1471](https://doi.org/10.1093/mnras/stv1471)
- Wuyts, E., Rigby, J. R., Gladders, M. D., et al. 2012, *ApJ*, 745, 86, doi: [10.1088/0004-637X/745/1/86](https://doi.org/10.1088/0004-637X/745/1/86)